Lateral capillary forces of cylindrical fluid menisci : an experimental, analytical and numerical study.

M. Mastrangeli, J.B. Valsamis, C. van Hoof, J.P. Celis, Pierre Lambert

Lateral capillary forces of cylindrical fluid menisci: an experimental, analytical and numerical study

M Mastrangeli[1,2], J-B Valsamis[3], C Van Hoof[1,4], J-P Celis[2] and P Lambert[3,5]

[1]IMEC, Kapeldreef 75, 3001 Leuven (BE)

[2]MTM Department, Katholieke Universiteit Leuven, Kasteelpark Arenberg 44, 3001 Leuven (BE)

[3]BEAMS Department, Université Libre de Bruxelles, Avenue F. D. Roosevelt 50, CP 165/56, 1050 Bruxelles (BE)

[4]ESAT Department, Katholieke Universiteit Leuven, Kasteelpark Arenberg 10, 3001 Leuven (BE)

[5]Femto-ST, CNRS UMR 6174, 24 rue Savary, 25000 Becançon (FR)

E-mail: mastran@imec.be

Abstract. Self-assembly and self-alignment driven by capillary meniscus forces are presently at the core of many important technological applications, including solder bonding in flip-chip assembly and fluidic self-assembly for microelectronic packaging. Lateral capillary meniscus forces were object of substantial theoretical and numerical modeling in recent years. Anyway, these studies were unsatisfactorily supported by direct experimental investigations. In this paper we present a comprehensive study of lateral capillary forces of cylindrical menisci, where experimental, analytical and numerical analyses of the same physical system are compared. We describe the conceptually simple experimental apparatus we designed to investigate lateral forces arising from small perturbations of cilindrical liquid menisci. The apparatus allowed controlling all physical and geometrical parameters relevant to the experiments. We then reproduce our experimental data with a novel analytical model of lateral fluid meniscus forces and with finite element simulations. The remarkable agreement between our experiments and models, while confirming earlier reports, provides a solid foundation for all applications of lateral capillary forces. Moreover, our experimental apparatus may be used as testbed for further experimental investigations of confined fluid menisci.

Keywords: Capillarity, self-assembly, self-alignment, analytical modeling, finite-elements modeling

PACS numbers:

AMS classification scheme numbers:

Submitted to: *Langmuir*

1. Introduction

Capillary and surface-tension-related phaenomena are ubiquitous in everyday life. Their thermodynamic origin lies in the minimization of the free energy of physical systems containing non-rigid interfaces [1, 2]. While being fundamental in bio-chemistry [3], capillary phaenomena are presently at the core of many technological applications as well, such as *e.g.* metallic bonding and soldering [4], microfluidics [5], switchable lenses [6], tightness systems [7] and precision manufacturing [8].

With specific respect to electronic manufacturing and packaging, the self-aligning motion of IC dies on top of substrates induced by the minimization of the interfacial energy of molten-solder bumps was first exploited by flip-chip assembly techniques to achieve passive yet highly-accurate die registration [9–12]. Capillarity is one powerful enabler of the three-dimensional deployment and actuation of articulated, hinged microelectromechanical structures of unprecedented complexity [13], and it is one of the physical mechanisms driving the growing class of packaging techniques based on self-assembly [14]. Surface-tension-driven self-assembly was first exploited for the construction of heterogeneous functional systems by the Whitesides Group [15–18]. It was later optimized and adapted to specific part-to-substrate assembly tasks by Srinivasan [19], Böhringer's group [20], Scott [21], Koyanagi's group [22, 23], Parviz's group [24, 25] and Jacobs' group [26, 27], to mention but a few examples.

All aforementioned electronic manufacturing techniques share, at least partly, the same underlying mechanism. Upon contact between the functional side (*i.e.* suitably pre-conditioned to enable further processing steps) of the part to be assembled (hereby representing *e.g.* IC die, microdevice, MEMS component) and the highly-energetic mating surface - normally composed by a fluid, such as *e.g.* hydrocarbons [19], water-based solutions [22] or molten solders [28] - of the corresponding binding site on the substrate, capillary forces - both perpendicular (*i.e.* axial) and parallel (*i.e.* lateral) to the substrate - act on the part and drive it to self-align with the underlying binding site [29]. The part, floating on the liquid meniscus, in this position achieves its rest (*i.e.* minimal energy) configuration. The same capillary forces intervene to oppose any sufficiently small displacement of the part from its rest position, and are therefore also referred to as *restoring* forces. The accuracy and degree of registration between part and binding site are mainly function of the lateral capillary forces, which in turn depend on many parameters, as evidenced in several studies briefly reviewed below. Axial capillary meniscus forces, investigated in details in [8], are further studied in a forthcoming publication [30].

Early theoretical investigations on lateral capillary forces aimed at predicting - both analytically and numerically - the shapes and corresponding self-aligning performance of fluid drops (representing *e.g.* molten-solder bumps) vertically-constrained by parallel plates and laterally-confined by the geometrical patterns, with constrasting wetting properties, of the same plates [31–33]. Finite elements, quasi-static numerical simulations - commonly performed using the powerful freeware Surface Evolver (SE) [34] of demonstrated reliability [35] - of such archetypical physical system - where the top plate is normally represented by a part of finite dimensions with all translational and rotational degrees of freedom free - later confirmed and further illustrated the dependency of lateral capillary forces on the physical properties of the fluid meniscus and on the geometry of the confining, planar geometrical patterns [36, 37]. Briefly, the forces are proportional to the surface tension of the fluid and inversely proportional to the height of the meniscus (also referred to as the *gap* in the following). Moreover, the magnitude of the lateral forces follow the (a)symmetry of the patterns of the confining sites; namely, they depend on the direction of the perturbation of

the meniscus (*i.e.* displacement of the top part) from its rest configuration as compared to the sides of the confining planar patterns: forces arising from displacements along shorter sides are stronger. Interestingly, Böhringer proposed a geometrical model that, while capturing many known properties of confined capillary menisci, greatly simplified energy and force calculations [38]. Built around the two-dimensional convolution of the patterns of the confining surfaces, the model easied the theoretical investigations on geometry-dependent self-alignment performance of binding sites [39, 40]. Nonetheless, being essentially two-dimensional, Böhringer's model accurately matches earlier results only for part displacements from the rest position larger than the meniscus height. Thus it cannot be used to model the alignment performance when in close proximity to the rest position - which is conversely of utmost importance in flip-chip-like assembly of parts with very small interconnection pitches. Particularly, the model neglects the curvature of the surface of the fluid meniscus, which particularly affects the capillary restoring forces for small meniscus perturbations [36, 41]. Given fixed geometrical boundary conditions, the meniscus curvature is directly influenced by the volume of the fluid: hence the need for accurate fluid volume control to achieve high process reliability and reproducibility [42].

As compared to the extensive modeling literature, experimental investigations on lateral capillary forces are up to now rare and overall unsatisfactory. Few works reported on the determination of the alignment accuracy achievable between part and binding site by means of capillary self-alignment, either optically [19, 43, 44] or analyzing assembly cross-sections by scanning electron microscopy [45]. Best claimed figures are of the order of $1\mu m$ or lower, which are amenable to the aforementioned packaging applications. Other researchers [46, 47] were able to estimate the maximum adhesion force binding flat parts onto fluid drops by recording the velocity of the fluid flow that caused the detachment of the parts in blowing tests [48]. Though these may be assumed as reasonable estimates of the maximal lateral capillary restoring forces of the menisci, we remark that in such conditions, where the direction of displacement of the floating part is not constrained to be parallel to the substrate, the measured values may hardly be entirely attributed to lateral force components. To our knowledge, only Zhang reported in literature experimental measurements and numerical simulations of lateral capillary forces arising from the same physical system [49]. The system was composed by a 450 μm x 250 μm flat silicon piece floating on a matching rectangular site confining a thin fluid drop - all immersed in water. The measurements of lateral capillary forces were performed in situ by means of a dedicated micromachined optical encoder, featuring laser-illuminated, calibrated optical gratings and a horizontal probe that displaced the part from its rest position in a direction parallel to the substrate. Anyway, though the proposed numerical model show reasonable match with experimental data, no mention is to be found of *e.g.* surface tension and volume of the fluid and meniscus height, which are pivotal parameters to reproduce and eventually appreciate the numerical results. Moreover, while their optical apparatus is very elegant, the way the physical system is set up is essentially stochastic, difficult to control and reproduce. By the same token, only one measurement is presented.

In this paper we present a comprehensive study of lateral capillary meniscus forces where experimental, analytical and numerical results of analyses on the same physical system are presented and compared. We describe the conceptually-simple experimental setup that we designed to quasi-statically measure the lateral restoring forces arising from fluid menisci of known physical and geometrical properties confined between two parallel plates. While easy to use being macroscopic, our setup still allows to control the position of the movable bottom plate with $1\mu m$ accuracy, and it can resolve forces as low as about $1\mu N$. By fixing the confining pads diameters and the meniscus height beforehand, our setup allows for reproducible experiences. The experimental results obtained

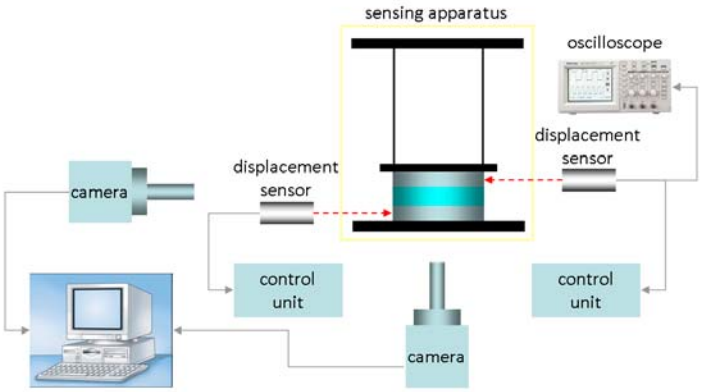

Figure 1. Schematic representation of the experimental setup used in this work. Relative dimensions are out of scale for representation purposes.

for circular pads (*i.e.* cilindrical fluid menisci) are then supported with good accuracy by both a simple analytical model, predicting restoring forces for small displacements of cilindrical fluid menisci, and by a SE model of the same system. In view of our results, our setup may constitute a referential testbed for further investigations on confined fluid menisci.

2. Experimental measurement of lateral capillary meniscus forces

2.1. The experimental setup

In designing our measurement apparatus, we tried to satisfy several requirements at once. 1) We wanted it to be simple and easy to use, yet allowing precise spatial manipulation: we aimed at macroscopic apparatus with micrometric spatial resolution; 2) the apparatus had to enable carefully-controlled and reproducible experiences: all relevant meniscus parameters of each experiment had to be reliably known (before or after the experiment itself); 3) we were interested in measuring lateral forces of the same order of magnitude of those arising in the technological applications of our interest, *i.e.* forces reportedly of the order of tens of μN [37]: this required both the use of an upscaled version of the physical system described in Section 1 (to keep up with point 1) that could still give rise to such forces, and the design of a correspondingly-sensible apparatus, *i.e.* able to reliably resolve few μN at maximum; 4) we were interested in lateral capillary forces only: the apparatus had to constrain the perturbation of the fluid meniscus to develop only in the direction parallel to the top and bottom surfaces confining the meniscus, and it had to exclude interferences from the axial component of the capillary force; 5) we were mainly interested in sampling the capillary force-versus-lateral displacement characteristic of the fluid meniscus close to its rest position: the imposed displacement had to amount to a small fraction of the height of the menisci only. Finally, 6) the fluids to be used had to have low volatility, so to allow for quasi-static, possibly long measurements without time-dependency of the fluid volume due to sustained fluid evaporation.

A schematic diagram and the actual implementation of the experimental setup are shown in Fig 1 and Fig. 2, respectively. The actual system under investigation was composed by two equal

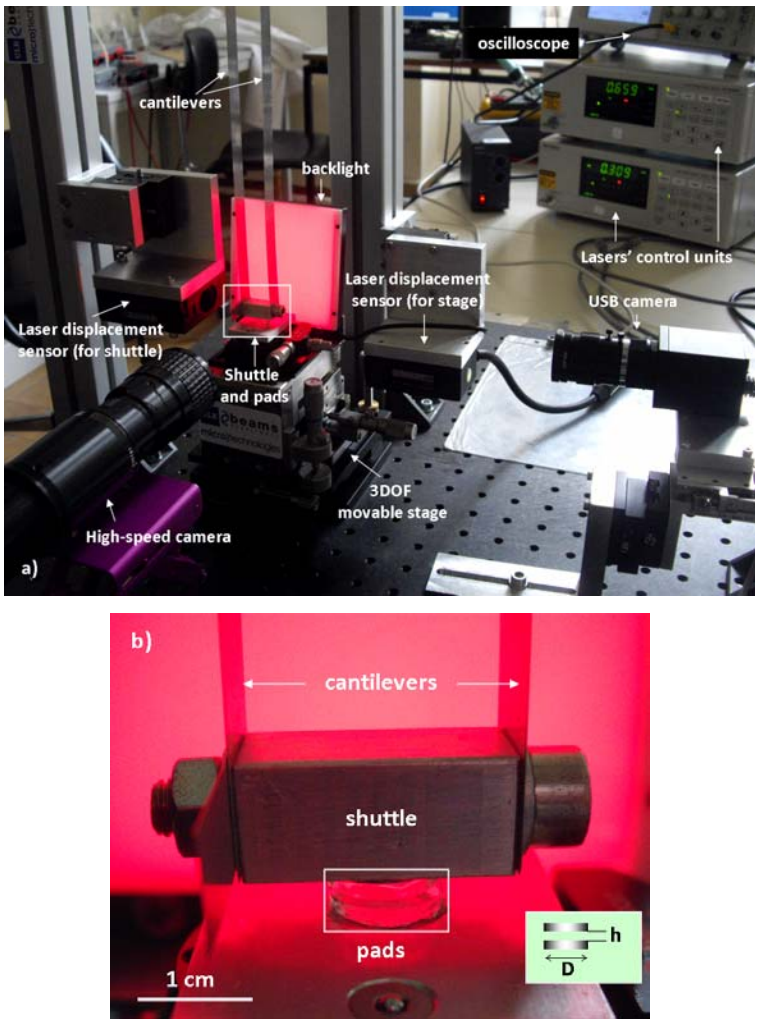

Figure 2. a) The experimental setup used in this work. A closeup view of the inset is shown in b), whose inset is further enlarged in Figure 4a.

glass cylinders of known dimensions (diameter $D = 2 \cdot R = 9.4mm$, thickness $t = 1.6mm$) which were used to vertically and laterally shape and confine the liquid menisci. The bottom cylinder was rigidly attached to a stage - anchored to the underlying table - that could be manually moved along all 3 translational degrees of freedom with micrometric precision (Newport M-562-XYZ). The lateral position of the movable stage was tracked by a laser displacement sensor (Keyence LC-2440) featuring a linear output characteristic for a displacement range of 3 mm within the interferometer's optimal working distance (3 cm from the laser source). The sensor's controller unit (Keyence LC-2400W) displayed calculated displacements (either absolute or relative to a prefixed position) in real time, and allowed direct filtering and averaging operations on acquired signals. The top cylinder was

Name	Density $[Kg/m^3]$	Viscosity $[Pa \cdot s]$	Surface Tension $[N/m]$	Supplier
Water	1000	0.001	0.072	Tap water
Oil 5	934	0.0093	0.0201	Dow Corning DC200FLUID10
Oil 6	960	0.096	0.0209	Dow Corning DC200FLUID100
Oil 1	970	0.485	0.0211	Rhodorsil R47V500
Oil 7	971	0.971	0.0212	Dow Corning DC200FLUID1000
Oil 2	973	4.865	0.0211	Rhodorsil R47V5000

Table 1. Fluids used in the experiments.

rigidly attached to the bottom surface of a machined aluminum parallelepiped (hereby referred to as the *shuttle,* of mass $m_{sh} = 12.748g$ including the top pad) featuring finely-smoothed surfaces, which in turn was held by two, equal blades of certified dimensions (feeler gage in close grain high carbon spring steel, Precision Brand) and mass $m_b = 2 \cdot 2.85g$ hanging from an overarching solid bridge (not shown). Upon attachment of the coupled blades to the bridge, the sliding motion of the shuttle (*i.e.* the bending motion of the blades) was constrained to take place exclusively along the single (lateral) direction where the measurements of displacement were performed. This double-cantilever-supported shuttle constituted the actual sensing device of the apparatus, and is hereby referred to as the *spring* for conciseness. The lateral position of the shuttle was tracked by an independent, dedicated laser displacement sensor (and control unit), identical to the aforementioned but pointing in the opposite direction. The vertical position of the (shuttle, and consequently of the) top pad was kept fixed throughout all the experiments, *i.e.* the hanging point and the lenght of the cantilevers holding the shuttle were never changed after initial calibration (described in the next Section) in order to consistently dispose of exactly the same sensing device in all experiences. Also, from this fixed boundary condition it followed that: 1) the vertical distance between the glass cylinders, *i.e.* the height h of the fluid menisci, could be precisely set at the beginning of each experiment using only the controlled vertical motion of the bottom stage; and that 2) the axial components of the capillary force were excluded from measurements, as desired, being balanced by the vincular reactions of the rigid supports. To inspect and set the initial, relative pad alignment, the plane parallelism of the surfaces of the pads and the initial profile of the fluid menisci, the positions of the top and bottom pad were visually tracked by two cameras connected to PCs: an USB camera pointed along the direction of lateral motion of the shuttle, and a high-speed camera (Photron Fastcam SA3 120K) pointed along the direction perpendicular to the previous and intersecting it in correspondence with the initial position of the bottom pad. The pads were illuminated by a flat backlight (LDL-TP-83x75, with PD-3012 power supply unit, CCS) with very-uniform light emission profile. This visual tracking setup easied the process of the alignment of the pads (see next Section). Pictures of the menisci were taken with the high-speed camera at the beginning (*i.e.* after complete meniscus trimming, described below) and at the end of every experiment to check whether the volume of the meniscus eventually changed during the measurements. The 1024 pixels-wide pictures spanned a field of view of about $20mm$, providing a resolution (and positioning accuracy) of about $20\mu m$.

All the experiments were performed in a laboratory environment; room temperature varied between 25^o and 28^o C, monitored relative air humidity was about 38%. Different liquids were used, whose properties are summarized in table 1.

The corresponding capillary lenght $L_c = \sqrt{\frac{\gamma}{\rho g}}$ of the oils was about $1.485mm$. In all experiments, the heights of the tested cylindrical menisci were smaller than L_c, so that gravity could be neglected as compared to capillary forces. For each fluid, we performed a series of experiments with progressively smaller meniscus heights. In the first experiment of each series, the meniscus height was calibrated to exactly $1mm$ by means of a ceramic slip gage (Mitutoyo) of known thickness. The contact angle [1] of silicon oils θ_{oil} on glass surfaces is rather small (about 20 degrees). This put a geometric constraint on the maximum allowed perturbation of the fluid meniscus (*i.e.* maximum displacement of the top pad relative to the bottom pad) to avoid fluid overflow beyond the edges of the bottom pad and consequent change of the volume of the fluid meniscus (see Section ?). Nevertheless, the range of allowed top pad relative displacements was fully coherent with our focus on small lateral meniscus perturbations. In some explorative experiences we also used water as meniscus fluid ($\gamma = 72mJ/m^2$, $L_c = 2.72mm$); as expected, its high volatility made our quasi-static measurements problematic and difficult to reproduce and model (see Section 5). The fluids were dispensed between the pads. Though not very precise, due to hardly-controllable tip pinch-off effects, we could not dispose of any dispensing method other than manual pipetting from calibrated pipettes. Because of this intrinsic dispensing imprecision, we calculated the actual volumes V and height h of the fluid menisci by offline MATLAB®-based post-processing of the pictures taken at the beginning of the experiments. Our semi-automatic, numerical algorithm computed V, h and D for each experiment (see [30] for more details). The exact calibration of the images was done using the $1mm$-thick ceramic gage, leading to a resolution of $14.2\mu m/pixel$. The numerical volume calculation was facilitated by the assumption of axisymmetric meniscus geometry - a constraint that we experimentally enforced in every experience: for each dispensed fluid drop, we purposely set the vertical position of the bottom pad in order to obtain a perfectly cylindrical meniscus profile (which is also assumed in the analytical model, see Section 4), as judged by visual camera inspection (see *e.g.* Fig. 4a). We made 3 numerical estimates for each experiment, and we discarded all experiments for which we could not get a ratio between the average values of V and h and their standard deviation larger than 10. To give an order of magnitude, the uncertainty on the heights was typically 2 pixels, *i.e.* about $28\mu m$. Thus we kept the heights of the menisci always higher than $280\mu m$ - which was not hard to do given the much larger diameter of the pads. Moreover, by comparing the reconstructed value of D to its measured value we could assess the accuracy of the estimates (see *e.g.* Table 3).

We remark that, though our experiments focused on circular pads only, lateral capillary forces arising from fluid menisci shaped by pads of arbitrary geometries can in principle be measured with our setup - though the exact knowledge of the dispensed fluid volume may be harder to get for non-axisymmetric menisci.

2.2. The working principle

The working principle of the sensing apparatus is sketched in Fig. 3, together with the local frame of reference. The initial conditions of each experiment were defined by manually trimming the fluid meniscus. The in-plane position of the bottom pad was set to be aligned with that of the top pad as judged by visual camera inspection: complete alignment (*i.e.* vertical superposition of the centers of both pads, with respective coordinate x and u) was reached when both, perpendicular cameras showed alignment of the edges of both pads. Then the vertical position of the bottom pad was manually set so to get a cylindrical profile, as previously discussed (Fig. 4a). In this condition, both the fluid meniscus and the spring were in their rest configurations: consequently,

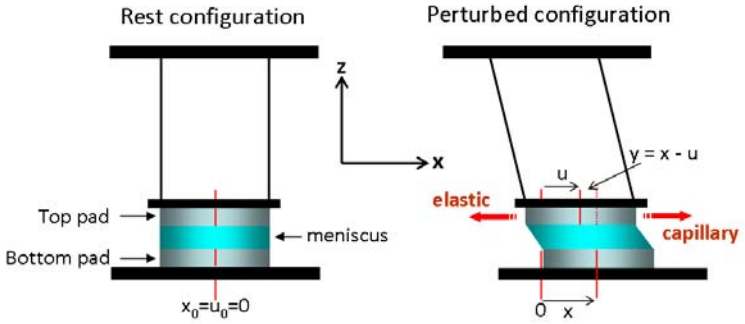

Figure 3. The working principle of our sensing device, based on the balance between capillary and elastic forces. Relative dimensions are out of scale for illustration purposes. (Actual examples of rest and perturbed configurations are shown in Fig. .)

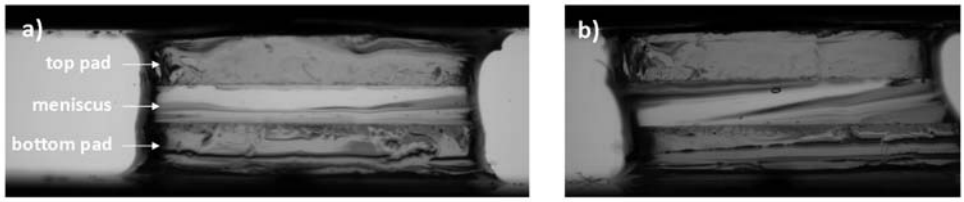

Figure 4. Experimental measurement of lateral capillary forces of a cylindrical meniscus. a) Rest configuration. Top and bottom pad are visually aligned, and the height of the meniscus ($1.205\mu m$) is trimmed to get a cylindrical profile. b) Perturbed configuration. After imposing a displacement ($x = 812\mu m$) to the bottom pad, the lateral force balance between capillary and elastic spring forces determines the equilibrium displacement of the top pad ($y = x - u = 660\mu m$ relative to the bottom pad).

both interferometers were reset to null relative displacement, to define the reference starting position (*i.e.* $x_0 = u_0 = 0$).

The measurements were then performed by imposing a known lateral displacement x to the bottom pad, as tracked by the dedicated sensor (Fig. 4b). This lateral shift perturbed both the fluid meniscus and the spring from their respective rest positions. As a consequence, two opposing lateral forces acted on the top pad: the capillary force tending to restore the meniscus rest position, and the elastic force tending to restore the shuttle rest position. The equilibrium of the lateral forces - achieved after some settling time, dependent on the viscosity of the fluid and the velocity of the movement of the shuttle - determined the actual displacement of the top pad: this was u (as tracked by the dedicated sensor) with respect to the rest position of the spring, and $y = x - u$ relative to the bottom pad. Hence, because of lateral force balance, the restoring lateral meniscus force corresponding to the net displacement u of the top pad relative to the bottom pad could be calculated by multiplying the absolute displacement u of the top pad times the bending stiffness of the spring - whose estimation is described in the next Section.

By imposing subsequent displacements to the bottom pad, we could experimentally sample

Estimation method	K $[N/m]$
Auxiliary cantilever - analytical	1.1506
Auxiliary cantilever - dynamic	0.9323
Auxiliary cantilever - weighting	1.0563
Dynamic	0.9375
Analytic	0.9036

Table 2. Summary of the estimates of the spring's bending stiffness.

the restoting force versus lateral displacement characteristic of our physical system. In all cases, displacements were imposed in both directions around the initial aligned position, in order to ascertain eventual asymmetries or histeretic phaenomena. From this curve, the stiffness of the fluid meniscus could be obtained by numerical polynomial fitting.

2.3. Bending stiffness of the spring

We estimated the bending stiffness K of our double-cantilever spring holding the shuttle at its sliding extremity in 3 different ways, obtaining a total of 5 estimates. All geometrical parameters of the spring were accurately known: beam lenght $L = 282mm$, thickness $h = 0.102mm$, width $b = 12.7mm$, total spring mass (including both beams, shuttle and top pad) $M = 18.448g$. Multiple alternative estimates were motivated mainly by the uncertainty on the effective Young Modulus E (standard assumed value: $210Gpa$) and density ρ (standard assumed value: $7800kg/m^3$) of our steel cantilevers, directly affecting our analytic estimates. A good agreement between all estimates was obtained - as summarized in Table 2 and detailed here below. Nonetheless, we tended to attribute higher confidence to the 2 fully-experimental estimates of K (defined below as $K_3$and K_4), which both avoid the guesses on E and ρ. Therefore, we assumed for the spring a bending stiffness equal to the average of K_3 and K_4, *i.e.* $K = 0.9969N/m$, with a relative uncertainty of 5.96%.

We remark that such high sensitivity enabled both the spring's desired high force resolution and its correspondingly-high susceptibility to environmental perturbations, discussed in Section 5.

2.3.1. The auxiliary cantilever method The first estimate involved an auxiliary steel cantilever of known dimensions (Precision Brand, length $l = 86.4mm$, thickness $h = 0.102mm$, width $b = 12.7mm$). The measurement principle exploited the lateral force balance between the cantilever and the spring (Fig. 5). Starting from the initial rest position, common to both cantilever and spring, a laser-tracked lateral displacement imposed on the cantilever induced a laser-tracked lateral displacement on the spring. After determining the bending stiffness of the cantilever, the stiffness of the spring was obtained from its force-versus-displacement curve (shown in Fig. 6) by polynomial fitting.

We estimated the bending stiffness k of the auxiliary cantilever in 3 ways. Assuming the standard stainless steel's Young's Modulus E and densityρ, the bending stiffness of a cantilever k is given analytically by [50]:

$$k = \frac{3EI}{L^3} \tag{1}$$

where I is the cantilever's second moment of inertia. We estimated I:

(i) Analytically, as $I = \frac{bh^3}{12}$. Inserting this in Eq.1 leads to $k_1 = 1.097N/m$.

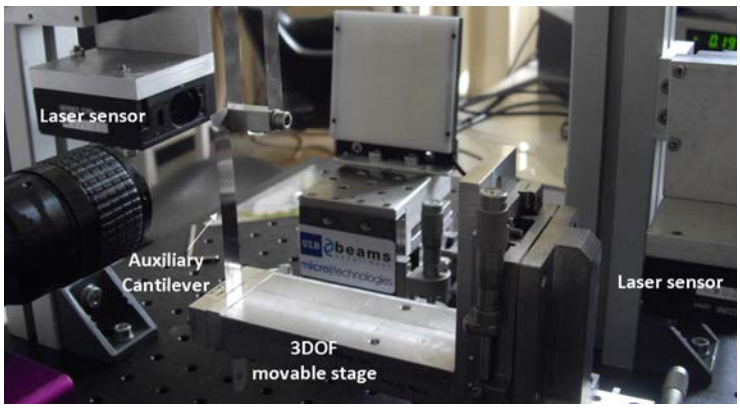

Figure 5. Experimental measurement of the stiffness of the spring by means of an auxiliary cantilever using lateral force balance.

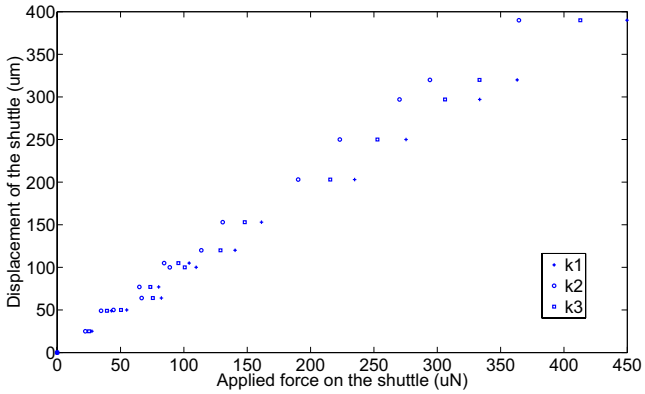

Figure 6. Displacement of the shuttle induced by the force applied on the shuttle by the auxiliary cantilever. 3 estimates for the applied force are given for each displacement value, according to the 3 estimated values of the cantilever stiffness $k_{\#}$(see text).

(ii) From the knowledge of the first resonance f_1 of the cantilever, as obtained by solving Euler's beam equation ([50], p. 273):

$$I = \frac{2\pi f_1 \rho}{E\beta_1^4} \tag{2}$$

where $\beta_1 = 1.875$. We measured the vibration period $t = 97ms$ of the cantilever analyzing its laser-tracked displacements on a digital oscilloscope. Hence, from Eqs. 2 and 1 we got $k_2 = 0.8889N/m$.

We also experimentally estimated the bending stiffness of the cantilever by measuring its point load-versus-point displacement characteristic (shown in Fig. 7) using several known loads. This gave us a value of $k_3 = 1.0071N/m$. We consider this the most reliable of our estimates of k.

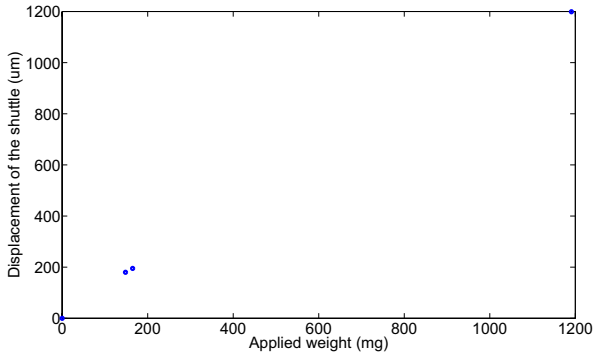

Figure 7. The displacement versus applied load used to calibrate the auxiliary cantilever.

Finally, from the measured force/displacement curve described above we consequently got a value of the bending stiffness $K_{\#}$ for each value $k_{\#}$: $K_1 = 1.1506N/m$, $K_2 = 0.9323N/m$ and $K_3 = 1.0563N/m$.

2.3.2. The dynamic method Knowing the natural oscillation frequency f_1 of the double-beam spring, its stiffness K_4 can be directly estimated according to:

$$K_4 = 4\pi^2 f_1^2 M_{eff} \tag{3}$$

where M_{eff} is the effective spring mass, including the mass of the shuttle and the kinetic energy-averaged mass of the cantilevers (according to Rayleigh method; see[50], p. 23, and Appendix A for details). The oscilloscope-measured natural frequency of the spring was $f_1 = 1.266hz$ which through Eq. 3 led to $K_4 = 0.9375N/m$.

2.3.3. The analytic method Finally, a fifth estimate of K was calculated fully analytically. We assumed that K_5 had 2 components: 1) the mechanical stiffness of 2 parallel, coupled cantilevers - with their unclamped extremities constrained by the shuttle to slide along a direction perpendicular to the cantilevers - given by material strength theory; and 2) a component due to the gravitational potential energy, which we converted into a so-called *gravitational stiffness.*

The mechanical component was obtained from:

$$K_{mech} = 2 \cdot \frac{12EI}{L^3} \tag{4}$$

We estimated the gravitational stiffness as (see Appendix B for details):

$$K_{grav} = \frac{6g}{5L}(m_{sh} + \frac{m_b}{2}) \tag{5}$$

where g is the acceleration of gravity. All parameters being known, we got a value of $K_5 = 0.9036/m$.

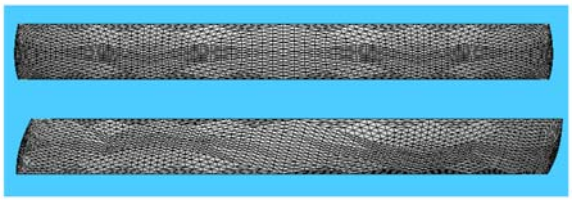

Figure 8. The Surface Evolver model of the fluid meniscus, for the case of experiment 2 defined in Table 3. The undeflected and maximal perturbation configurations (top pad displacement: $273\mu m$) are shown.

3. Finite element model

We modeled our experiments on cylindrical fluid menisci with Surface Evolver [34] (Fig. 8). The code was adapted from the *column* example wrote by SE's developer K. Brakke‡. All geometrical (radius of the pads R, meniscus height and volume as obtained by image post-processing for each experiment) and physical (fluid density and surface tension) parameters reproduced those of the experiments. We imposed the pinning of the fluid triple contact-line along all the circular edge of both pads - a condition that we enforced at the beginning of each experiment, as already said, and that was satisfied for all measurements of small meniscus perturbations, as judged by visual inspection. The capillary forces were calculated by the method of virtual works [50] using central differences. To define a reliable degree of mesh refinement, we tested our model until we got a satisfactory match against the benchmark given by the axial force produced by a perfectly cylindrical fluid meniscus, which is analytically given by $F = -\pi\gamma R$. In simulating the force-vs.-displacement curve of few of our experiences, we input the same relative displacements of the top relative to the bottom pad that were measured in the experiments. We finally extrapolated the simulated lateral stiffness of the fluid meniscus by polynomial fitting of the curve.

4. Analytic model

We developed an analytical model to estimate the lateral stiffness of a cylindrical meniscus confined between two circular pads. Perfectly-cilindrical meniscus profiles were assumed for analytical closed-form tractability, though such assumption is ideal and not always satisfied in experimental conditions.

We firstly computed the lateral area of a tilted cylinder of height h, radius R and relative shift between pads u (see Fig. 9 for the definition of the geometrical parameters). In this configuration, the cylinder axis is not perpendicular to both circles but inclined with an angle α given by $\tan\alpha = u/h$.

The equation of this cylinder is given by:

$$S \equiv \bar{OP} = z\bar{1}_z + u(z)\bar{1}_x + R\bar{1}_r \tag{6}$$

$$= (\frac{z}{h}u + R\cos\theta)\bar{1}_x + (R\sin\theta)\bar{1}_y + z\bar{1}_z \tag{7}$$

Computing the area element dS as:

$$dS = \|\bar{N}\| \tag{8}$$

‡ The code is available at http://www.susqu.edu/brakke/evolver/html/column.htm

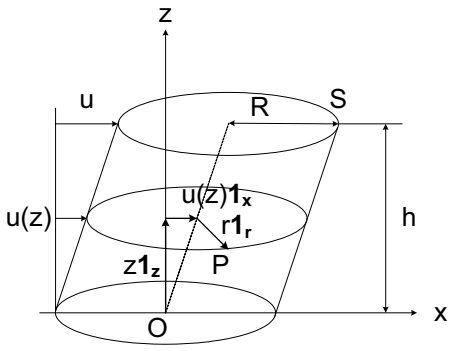

Figure 9. Geometry of a fluid meniscus confined between circular parallel pads. h, radius R. The offset bewteen both circular pads is u.

with $\bar{N} = \frac{\partial \bar{S}}{\partial \theta} \times \frac{\partial \bar{S}}{\partial z}$, we finally find:

$$dS = R\sqrt{1 + \cos^2\theta \frac{u^2}{h^2}} \tag{9}$$

The lateral area is consequently equal to:

$$S = R \int_0^h dz \int_0^{2\pi} \sqrt{1 + \cos^2\theta \frac{u^2}{h^2}}\, d\theta \tag{10}$$

Using the well-known approximation $(1+x)^n \approx 1 + nx$ for small x, we replace the square root by $1 + \frac{1}{2}\frac{u^2}{h^2}\cos^2\theta$, which finally leads to:

$$S \approx 2\pi R h (1 + \frac{u^2}{4h^2}) \tag{11}$$

Since the total (variable) energy of the system is here equal to:

$$E = \gamma S \tag{12}$$

(where γ is the surface tension), the lateral restoring force is equal to:

$$F = -\frac{\delta E}{\delta u} = -\pi R \gamma \frac{u}{h} \tag{13}$$

which correspond to a constant stiffness k given by:

$$k = \frac{\delta F}{\delta u} = \frac{\pi R \gamma}{h} \tag{14}$$

This formulation was benchmarked using our Surface Evolver model, in the case of $r = 50\mu m$, $h = 70\mu m$, $\gamma = 0.325 N/m$ and a volume of liquid given by $V = \pi r^2 h$. The comparison is plotted in figure 10. Good agreement between the models was achieved for small relative shifts (*i.e.* small u/h values) - which are coherent with those induced in our experiments.

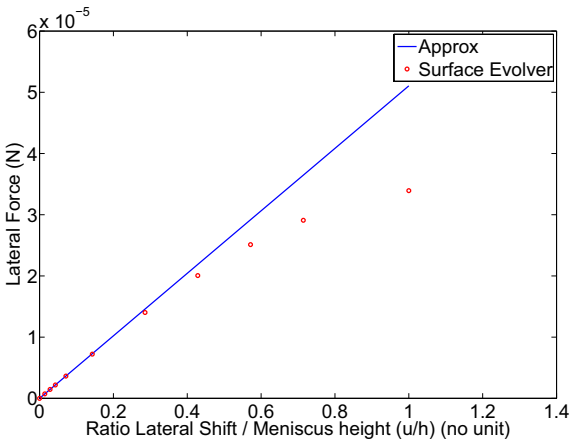

Figure 10. Comparison of analytical and numerical (SE) results for the benchmark configuration with$R = 50\mu m$, $h = 70\mu m$ and $\gamma = 0.325N/m$.

5. Results and discussion

When performing the experiments, the magnitude of the successive displacements along the curve was empirically determined as a compromise between the competing needs to accurately sample the curves and to avoid as much as possible the effects of environmental noise. The spring was indeed as sensible as to be clearly perturbed by the movement of the surrounding air. This was the main source of noise, together with the vibration of the movable stage (induced by floor vibrations, though partly-attenuated by an absorbing plastic layer set underneath the apparatus). As a consequence, the spring could eventually undergo stochastic swinging movements as large as few tens of micrometers before settling to the equilibrium position imposed by the boundary conditions. To cope with this: 1) we spaced the successive positions of the bottom pad $50\mu m$ apart; 2) we moved the bottom pad pretty slowly in between the prefixed positions to avoid inducing excessive air and fluid flows, and we waited up to several tens of seconds after each prefixed position was reached to let the transient phaenomena (in the air and in the meniscus) estinguish; and 3) we applied the maximum number of measurement averages (131072) on the incoming signals available in the units controlling both laser sensors, to cancel out fluctuations and thus achieve the maximal force resolution possible. On the other hand, such relatively wide spacing between sampling point, as compared to the full range of imparted displacements, made no harm to faithfully reconstruct the desired curves: close to the origin, the behavior of the fluid menisci was indeed expected to be linear [36, 37] - as we experimentally confirmed it to be *a posteriori*.

Table 3 and Fig. 11 show a summary of results of our investigations. We performed a total of 34 experiments; however, we report for comparison only those experiments for which 1) no fluid overflow nor sensible evaporation took place, and 2) the estimates of volumes and heights of the menisci were accurate (according to criteris discussed in Section 2.1). The lateral stiffness of several cylindrical fluid menisci, as resulting from experiments and both the analytic and numerical models, are thereby shown together with the physical and geometrical boundary conditions of each case and the relative errors in the estimates. As an example, Fig. 12 shows the specific capillary force-versus-

Experiment	Geometry	Fluid	K $[N/m]$	Modeling error
1	height: $1.138mm$	Oil 2	Exp: 0.2466	
	volume: $85.6nL$		SE: 0.2415	$2,07\%$
	diameter: $9.186mm \pm 2.28\%$		An: 0.2797	13.42%
2	height: $1mm$	Oil 6	Exp: 0.2827	
	volume: $74.2nL$		SE: 0.294	3.99%
	diameter: $9.63mm \pm 2.45\%$		An: 0.3152	11.48%
3	height: $0.852mm$	Oil 6	Exp: 0.3392	
	volume: $57.1nL$		SE: 0.3456	1.89%
	diameter: $9.41mm \pm 0.11\%$		An: 0.3698	9.01%
4	h: $1mm$	Oil 2	Exp: 0.2407	
	V: $65.5nL$		SE: 0.2648	10.01%
	D: $9.29mm \pm 1.21\%$		An: 0.3182	32.19%
5	h: $0.906mm$	Oil 2	Exp: 0.2962	
	V: $54.2nL$		SE: 0.3285	10.90%
	D: $9.15mm \pm 2.64\%$		An: 0.351	18.50%
6	h: $0.720mm$	Oil 2	Exp: 0.3485	
	V: $47.3nL$		SE: 0.3989	14.46%
	D: $9.44mm \pm 0.42\%$		An: 0.4417	26.75%

Table 3. Summary of results (Exp = experimental, SE = Surface Evolver, An = analytical). The relative errors of the the SE and An models compared to the experimental estimates are shown in the last column. The relative error in the reconstruction of the pad diameter by the image post-processing algorithm was used to assess the accuracy of the estimates on meniscus heights and volumes.

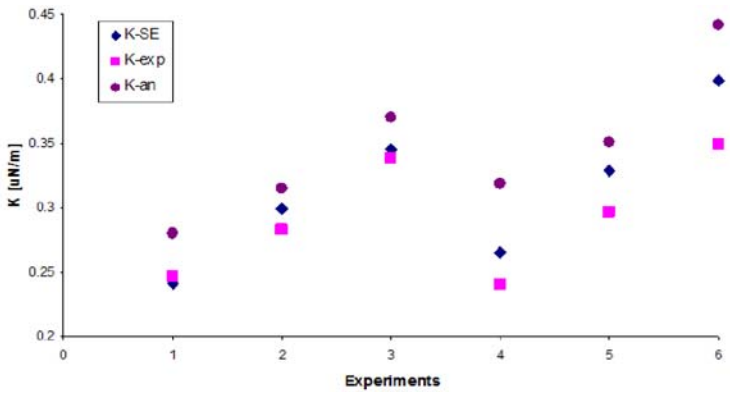

Figure 11. Comparison of lateral stiffness of 6 measured cylincrical menisci (see Table 3), as resulting from experimental data and numerical and analytical models.

lateral displacement characteristic relative to the second experiment reported in Table 3, with both experimental and modeling data.

The experimental results confirm that lateral capillary forces arising from cylindrical menisci of lower height (which, because the procedure we adopted, means correspondingly lower volumes)

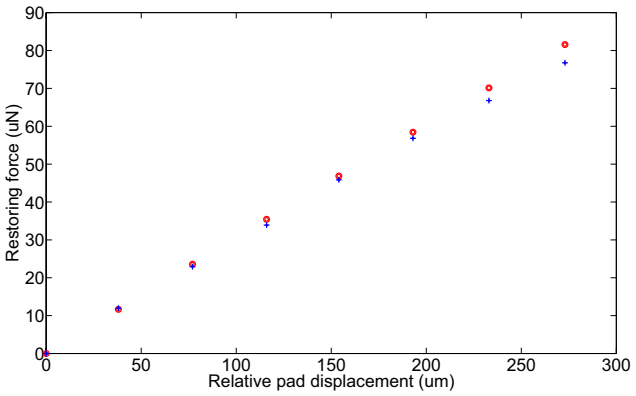

Figure 12. Experimental and numerical (SE) results for experiment 2 in Table 3.

are proportionally larger. Furthermore, the general trend apparent from comparison of the results is that both SE and analytical models tend to overestimate the meniscus stiffness, with the SE estimate closer to the experimental values. Also, the relative errors of analytical estimates (up to 32%, with an average of 18.6%) are larger than those of the numerical model (up to 14%, with an average of 7.2%). We attribute this to several factors and sources of errors.

5.1. Sources of error

The relative error on the reconstructed value of pad diameters D (shown in the last column of Table 3) can be assumed to be an indication of the error on the estimates of volumes and heights of the menisci. These errors in turn directly affect the geometry of the menisci, and thus both models' estimates of their lateral stiffness. Indeed, given the relative errors δh and δR on the estimates of h and R, respectively, the relative error on the volume of a cylinder is:

$$\frac{\delta V}{V} = \delta h + 2 \cdot \delta R \tag{15}$$

which equals $3 \cdot \delta R$ assuming equal relative errors for h and R. Considering *e.g.* the case of experiment 2, with reference parameter and error values shown in Table 3, the effects of relative errors on h, D and V give a relative error on the simulated versus experimental values of meniscus stiffness of 8.6% (augmented case) and 7.62% (dimished case), respectively. Thus, this and similar error propagation analyses make the relative error between SE data and real data more plausible, and may partly explain it. By the same token, we also remark that the relative uncertainty on the experimental value of the stiffness of the spring ($\sim 6\%$) is by itself close to the average relative error of the SE model compared to experiments (7.2%).

Relative errors on estimates of D do also affect, though to a lesser extent, the estimates for k resulting from the analytical model. However, with this regard we can further assume *a posteriori* that the axysimmetric meniscus geometries we tried to enforce by visual inspection at the beginning of each experiment were still not perfectly cilindrical; we think this may be the main reason of the systematic analytical overestimates of the stiffnesses of the menisci.

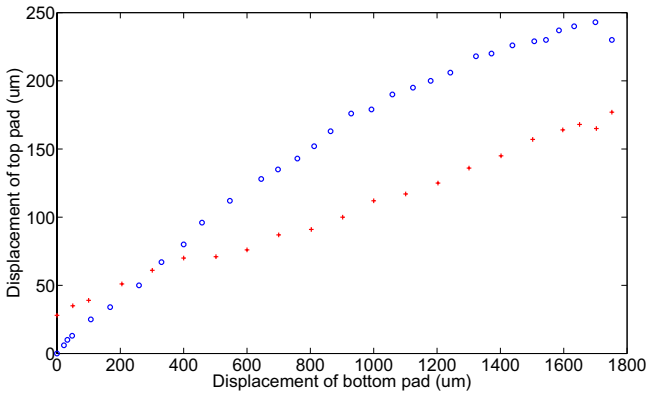

Figure 13. Experimental top pad-versus-bottom pad (*i.e.* x_T vs. x_B) displacement curve in presence of hysteresis (circles: forward scan (increasing displacements), crosses: backward scan). The large top pad displacement induced the fluid overflow over the edge of the bottom pad, changing the volume and the profile of the meniscus, and consequently the magnitude of the restoring force.

Furthermore, in both models we used the values of fluids' surface tensions γ given by the providers. It cannot be excluded that adsorbtion of contaminants from air during the experiments might have made the actual values different from the nominal ones, especially for long experiments. A change in γ would proportionally affect the restoring forces, thus the stiffnesses of the menisci.

In view of all these plausible sources of errors, we consider the matching between our models and experiments to be satisfying.

5.2. Hysteresis

Fig. 13 shows the results of one early experiment, where relatively-large top pad displacements were induced on a oil meniscus. Comparing the forward and the backward curves, a clearly hysteretic behaviour was seen. This was due to the overflow of the fluid beyond the edge of the bottom pad. This happened when the angle between the surface of the meniscus on its advancing side and the surface of the bottom pad was larger than

$$\theta_{max} = \theta + 180^o - \phi \tag{16}$$

ϕ being the angle between the bottom pad surface and its side surface (equal to 90^o in our case) [51]. Beyond this value of that angle, the fluid was no longer confined by the rim of the pad and it wet the vertical side of it, overflowing (Fig. 14a). The overflow changed the residual amount of fluid in the meniscus. The profile of the meniscus during the backward movement was thus different compared to the forward movement, hence the difference in the resulting restoring force. Depending on θ and the actual height h of the meniscus, fluid overflow could be avoided by keeping the displacement of the top relative to the bottom pad below $y_{max} = h \cdot \tan(\theta)$ (Fig. 14b). For a typical case with $h = 1mm$ and $\theta = 20^o$, we get a limit value of $364\mu m$.

We incidentally observe that, thanks to 1) the aforementioned geometrical relation (Eq. 16), and 2) the possibility to exactly track in real time the value of the relative displacement between top and bottom pad, our setup directly enables an alternative method (which we called the *overflow*

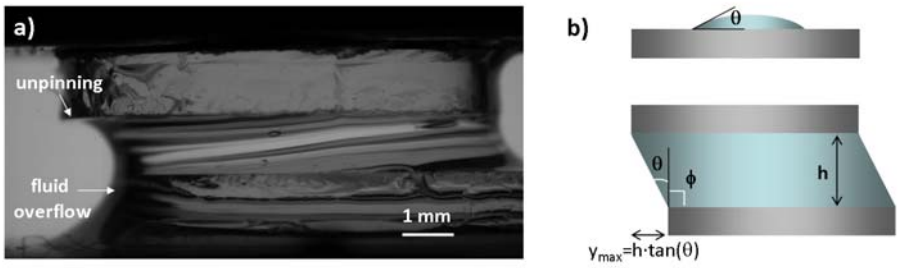

Figure 14. Hysteresis by large displacement of the top relative to the bottom pad (a). Beyond a geometrically-predictable value of displacement (*i.e.* of the advancing angle $\theta + 180 - \phi$ between the fluid and the bottom pad, as shown in b) the fluid is no longer confined on top of the bottom pad surface, and it overflows. The volume of the residual fluid confined between the pads is decreased, changing the profile of the meniscus. Triple contact-line unpinning along the edge of the top pad is also seen.

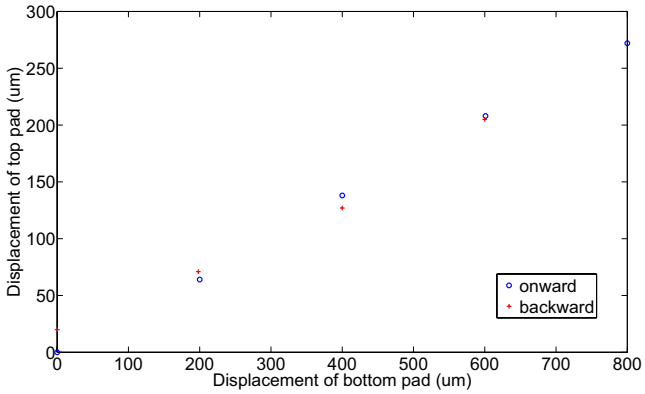

Figure 15. Hysteresis due to fluid evaporation during experimental measurements of relative pads displacements. A time-varying meniscus volume affects the restoring forces during onward and backward displacements.

method) to experimentally determine the contact angle of liquids on flat surfaces - eventually using non-circular pads. This novel method may be particularly useful for estimating very-small CAs, as they are "magnified" by the additional value $180^o - \phi$ due to the constrained geometry of the setup. Interestingly, for this collateral application no thorough calibration of the apparatus is necessary, apart from the synchronization of the laser and visual tracking system.

Hysteretical results were also seen when using water as fluid even applying only small displacements (see *e.g.* Fig 15). In this case the source of hysteresis was the rapid evaporation of water - that evidently affected the volume and thus the curvature of the meniscus - and/or the higher susceptibility of the water surface to adsoption of surfactants from air, which sensibly affect its surface tension.

6. Conclusions and future work

In this paper we presented a comprehensive study of lateral capillary forces arising from small perturbances of cylindrical menisci. We experimentally measured the restoring forces by means of a sensing apparatus of our design, operating on the principle of lateral force balance between capillary and elastic forces. We also presented a novel analytical model describing in closed-form the lateral stiffness of cylindrical menisci. The predictions of this model, together with those of a Surface Evolver model of the experimental system, showed a good match with the experimentally-measured values of the stiffnesses. We also discussed the sources of noise, error and hysteresis possibly affecting our sensing apparatus and/or intrinsic to such quasi-static type of experiments.

The possibility of tracking in real time and with micrometric accuracy the relative displacements of top and bottom pads of our system lets our apparatus enable the direct measurement of the contact angle of liquids on top of flat surfaces. This novel method exploits the sudden overflow of liquid over the edge of the confining bottom surface for sufficiently large perturbations of the meniscus profile. The validation of such *overflow* method, which may be useful particularly to measure rather small liquid contact angles, is currently being pursued.

Finally, our experimental apparatus could constitute a reference testbed to further investigate lateral capillary forces, arising from fluid menisci of even arbitrary profiles and shapes. The meniscus geometry can indeed be defined by the geometry of the confining pads - besides the other parameters discussed earlier. Scaling properties may be also investigated, as well as the self-alignment dynamics enabled by capillary forces, which is fundamental to many present-day technological applications and indeed object of a forthcoming publication of our research group [Lambert's dynamic paper].

Appendix A. The effective spring mass

The mass of the spring's 2 cantilever ($m_b = 5.7g$) was not negligible compared to that of the shuttle and top pad ($m_s = 12.778g$). Therefore, in the dynamic estimation of the spring's stiffness we introduced an equivalent mass for both beams m_{eq}, which would have the same kinetic energy as the actual cantilevers for the same shuttle velocity v according to:

$$\frac{1}{2}m_{eq}v^2 = 2 \cdot \frac{1}{2}\int_0^L v^2(z)dm' = 2 \cdot \frac{1}{2}\lambda \int_0^L v^2(\xi)d\xi \tag{A.1}$$

where $dm' = \lambda d\xi$, and λ has the dimension of mass per unit length. The velocity $v(z)$ of each cantilever element located at a distance z from the clamped extremity was assumed to be proportional to its displacement computed by material strength theory:

$$v(z) = \frac{q(z)}{u}v \tag{A.2}$$

where the element $q(z)$ is given by:

$$q(z) = \frac{F}{EI}\left(\frac{Lz^2}{4} - \frac{z^3}{6}\right) \tag{A.3}$$

and $u = q(L)$. Using Eqs. A.3, A.2, and 4 we get:

$$v^2(z) = v^2\left(\frac{9z^4}{L^4} - \frac{12z^5}{L^5} + \frac{4z^6}{L^6}\right) \tag{A.4}$$

which, inserted in Eq. A.1, leads to:

$$m_{eq} = \frac{13}{35} m_b \tag{A.5}$$

Finally, the effective spring mass M_{eff} is given by:

$$M_{eff} = m_{sh} + m_{eq} = 14.8171g \tag{A.6}$$

Appendix B. The gravitational stiffness

The gravitational component of the spring's stiffness arises from the fact that an horizontal displacement u of the shuttle is concurrent to a vertical parasitic motion p given by Henein ([52], formula 5.13) as:

$$p \approx \frac{3u^2}{5L} \tag{B.1}$$

Considering that the shuttle undergoes a p upward displacement while each beam's mass center undergoes a $p/2$ vertical displacement, the gravitation stiffness K_{grav} is defined as follows (m_b is the mass of the 2 cantilevers):

$$\frac{1}{2} K_{grav} u^2 = m_{sh} g p + m_b g \frac{p}{2} \tag{B.2}$$

which together with Eq. B.1 leads to Eq. 5.

Acknowledgments

This work was supported by the EU project HYDROMEL. The authors thank Bruno Tartini and Jean-Salvatore Mele for their valuable help in manufacturing.

References

[1] A. W. Adamson. *Physical chemistry of surfaces*. Wiley, 1990.

[2] P.-G. de Gennes, F. Brochard-Wyart, and D. Quere. *Capillarity and Wetting Phenomena: Drops, Bubbles, Pearls, Waves*. Springer, 2004.

[3] J. Israelachvili. *Intermolecular and surface forces*. Academic Press, 1994.

[4] R. J. K. Wassink. *Soldering in electronics*. Electrochemical Publications, 2005.

[5] M. Gad el Hak, editor. *The MEMS Handbook*. CRC Press, 1998.

[6] B. Berge and J. Peseux. Variable focal lens controlled by an external voltage: An application of electrowetting. *European Physical Journal E*, 3:159–163, 2000.

[7] M. De Volder, J. Peirs, D. Reynaerts, J. Coosemans, R. Puers, O. Smal, and B. Raucent. A novel hydraulic microactuator sealed by surface tension. *Sensors and Actuators A: Physical*, 123-4:547–554, 2005.

[8] P. Lambert. *Capillary forces in microassembly*. Springer, 2007.

[9] L. S. Goodman. Geometrical optimization of controlled collapse interconnections. *IBM Journal of Research and Development*, 13:251–265, 1969.

[10] C. Kallmayer, H. Oppermann, G. Engelmann, E. Zakel, and H. Reichl. Self-aligning flip-chip assembly using eutectic gold/tin solder in different atmospheres. In *IEEE International Electronics Manufacturing technology Symposium*, 1996.

[11] G. Humpston. Flip chip solder bonding for microsystems. *IEE Colloquium on assembly and connections in microsystem*, 1997.

[12] Q. Tan and Y. C. Lee. Soldering technology for optoelectronic packaging. In *IEEE Electronic Components and Technology Conference*, 1996.

[13] R. R. A. Syms, E. M. Yeatman, V. M. Bright, and G. M. Whitesides. Surface-tension powered self-assembly of microstructures the state of the art. *IEEE J. Microelectromechanical Systems*, 12:387–417, 2003.

[14] M. Mastrangeli, S. Abbasi, C. Varel, C. van Hoof, J.-P. Celis, and K. F. Bohringer. Self-assembly from milli- to nanoscale: methods and applications. *J. Micromech. Microeng.*, 19:083001, 2009.

[15] A. Terfort, N. Bowden, and G. M. Whitesides. Three-dimensional self-assembly of millimetre-scale components. *Nature*, 386:162–4, 1997.

[16] A. Terfort and G. M. Whitesides. Self-assembly of an operating electrical circuit based on shape complementarity and the hydrophobic effect. *Advanced Materials*, 10:470–3, 1998.

[17] M. Boncheva, D. A. Bruzewicz, and G. M. Whitesides. Millimeter-scale self-assembly and its applications. *Pure Appl. Chem.*, 75:621–630, 2003.

[18] M. Boncheva and G. M. Whitesides. Making things by self-assembly. *MRS Bullettin*, 30:736–742, 2005.

[19] U. Srinivasan, D. Liepmann, and R. T. Howe. Microstructure to substrate self-assembly using capillary forces. *IEEE J. Microelectromechanical Systems*, 10:17–24, 2001.

[20] X. Xiong, Y. Hanein, J. Fang, Y. Wang, W. Wang, D. T Schwartz, and K. F. Bohringer. Controlled multibatch self-assembly of microdevices. *IEEE J. Microelectromechanical Systems*, 12:117–127, 2003.

[21] K. L. Scott, T. Hirano, H. Yang, H. Singh, R. T. Howe, and A. N. Niknejadk. High-performance inductors using capillary based fluidic self-assembly. *IEEE J. Microelectromechanical Systems*, 13:300–9, 2004.

[22] T. Fukushima, Y. Yamada, H. Kikuchi, T. Tanaka, and M. Koyanagi. Self-assembly process for chip-to-wafer three-dimensional integration. In *IEEE Electronic Components and Technology Conference*, pages 836–841., 2007.

[23] T. Fukushima, H. Kikuchi, Y. Yamada, T. Konno, J. Liang, K. Sasaki, K. Inamura, T. Tanaka, and M. Koyanagi. New three-dimensional integration technology based on reconfigured wafer-on-wafer bonding technique. In *IEEE International Electronic Device Meeting*, pages 985–8., 2007.

[24] S. A. Stauth and B. A. Parviz. Self-assembled single-crystal silicon circuits on plastic. *Proc. Nat. Ac. Sc.*, 103:13922–7, 2006.

[25] C. J. Morris and B. A. Parviz. Micro-scale metal contacts for capillary force-driven self-assembly. *J. Micromech. Microeng.*, 18:015022 (10pp), 2008.

[26] W. Zheng and H. O. Jacobs. Self-assembly process to integrate and interconnect semiconductor dies on surfaces with single-angular orientation and contact-pad registration. *Advanced Materials*, 18:1387–1392, 2006.

[27] J. Chung, W. Zheng, T. J. Hatch, and H. O. Jacobs. Programmable reconfigurable self-assembly: parallel heterogeneous integration of chip-scale components on planar and nonplanar surfaces. *IEEE J. Microelectromechanical Systems*, 15:457–464, 2006.

[28] E. Saeedi, S. Abbasi, K. F. Bohringer, and B. A. Parviz. Molten-alloy driven self-assembly for nano and micro scale system integration. *Fluid Dynamics & Materials Processing*, 2:221–246, 2007.

[29] M. Mastrangeli, W. Ruythooren, C. Van Hoof, and J.-P. Celis. Conformal dip-coating of patterned surfaces for capillary die-to-substrate self-assembly. *J. Micromech. Microeng.*, 19:045015, 2009.

[30] J.-B. Valsamis, M. Mastrangeli, and P. Lambert. *forthcoming*, 2009.

[31] S. K. Patra and Y. C. Lee. Quasi-static modeling of the self-alignment mechanism in flip-chip soldering - part 1: single solder joint. *Journal of Electronic Packaging*, 113:337–342, 1991.

[32] S. K. Patra and Y. C. Lee. Modeling of self-alignment mechanism in flip-chip soldering - part ii: multichip solder joints. In *Proc. Electronic Components and Technology Conference*, 1991.

[33] B. Yost, J. McGroarty, P. Borgesen, and C.-Y. Li. Shape of a nonaxisymmetric liquid solder drop constrained by parallel plates. *IEEE Transactions on Components, Hybrids and Manufacturing Technology*, 16:523–6, 1993.

[34] K. A. Brakke. The surface evolver. *Experimental Mathematics*, 1:141–165, 1992.

[35] P. M. Martino, G. M. Freedman, L. M. Racz, and J. Szekely. Predicting solder joint shape by computer modeling. In *Proc. Electronic Components and Technology Conference*, 1994.

[36] W. Lin, S. K. Patra, and Y. C. Lee. Design of solder joints for self-aligned optoelectronics assembly. *IEEE Transactions on Components, Packaging and Manufacturing Technology - Part B*, 18:543–551, 1995.

[37] J. Lieneman, A. Greiner, J. G. Korvink, X. Xiong, Y. Hanein, and K. F. Bohringer. Modelling, simulation and experiment of a promising new packaging technology parallel fluidic self-assembly of microdevices. *Sensors Update*, 13:3–43, 2003.

[38] K. F. Bohringer, U. Srinivasan, and R. T. Howe. Modelling of capillary forces and binding sites for fluidic self-assembly. In *EEE International Conference on MEMS*, pages 369–374, 2001.

[39] S.-H. Liang, X. Xiong, and K. F. Bohringer. Toward optimal designs for self-alignment in surface tension driven micro-assembly. In *IEEE International Conference on MEMS*, pages 9–12, 2004.

[40] X. Xiong, S.-H. Liang, and K. F. Bohringer. Geometric binding site design for surface-tension driven self-assembly. In *Proc. IEEE International Conference on Robotics and Automation*, pages 1141–1148, 2004.

[41] N. Van Veen. Analytical derivation of the self-alignment motion of flip-chip soldered components. *Transactions of the ASME*, 121:116–121, 1999.

[42] M. Mastrangeli, W. Ruythooren, J.-P. Celis, and C. Van Hoof. Challenges for capillary self-assembly of microsystems. *submitted to publication*, 2009.

[43] K. Sato, K. Ito, S. Hata, and A. Shimokohbe. Self-alignment of microparts using liquid surface tension: behaviour of micropart and alignment characteristics. *Precision Engineering*, 27:42–50, 2003.

[44] K. Sato, K. Lee, M. Nishimura, and K. Okutsu. Self-alignment and bonding of microparts using adhesive droplets. *Int. Journal. Precision Engineering and Manufacturing*, 8:75–79, 2007.

[45] T. Fukushima, H. Kikuchi, Y. Yamada, T. Konno, J. Liang, K. Sasaki, K. Inamura, T. Tanaka, and M. Koyanagi. New three-dimensional integration technology based on reconfigured wafer-on-wafer bonding technique. In *IEEE International Electronic Device Meeting*, 2007.

[46] R. W. Bernstein, X Zhang, S. Zappe, M. Fish, M. Scott, and O. Solgaard. Characterization of fluidic microassembly for immobilization and positioning of drosophila embryos in 2-d arrays. *Sensors and Actuators A*, 114:191–6, 2004.

[47] C. Lin, F. Tseng, and C.-C. Chieng. Studies on size and lubricant effects for fluidic self-assembly of microparts on patterned substrates using capillary effect. *Journal of Electronic Packaging*, 130:021005–1, 2008.

[48] C. D. Cooper and F. C. Alley. *Air pollution control: a design approach.* Waveland, 1994.

[49] X. Zhang, C.-C. Chen, R. W. Bernstein, S. Zappe, M. P. Scott, and O. Solgaard. Microoptical characterization and modeling of positioning forces on drosophila embryos self-assembled in two-dimensional arrays. *IEEE J. Microelectromechanical Systems*, 14:1187–1197, 2005.

[50] W. T. Thomson and M. D. Dahleh. *Theory of vibration with applications.* Prentice Hall, 1998.

[51] R. Seemann, M. Brinkmann, E. J. Kramer, F. F. Lange, and R. Lipowsky. Wetting morphologies at microstructured surfaces. *Proc. Nat. Acc. Sc.*, 102:1848–1852, 2005.

[52] S. Henein. *Conception des structures articulées à guidages flexibles de haute précision.* PhD thesis, Ecole Polytechnique Federale de Lousanne, 2000.